Ocean Systems Engineering, *Vol. 9, No. 2 (2019) 111-133*
DOI: https:// doi.org/10.12989/ose.2019.9.2.111

Optimization of a horizontal axis marine current turbine via surrogate models

Karthikeyan Thandayutham[1], E.J. Avital[2],
Nithya Venkatesan[3] and Abdus Samad[*1]

[1]*Wave Energy and Fluids Engineering Laboratory (WEFEL), Department of Ocean Engineering, Indian Institute of Technology Madras, Chennai, India*
[2]*School of Engineering and Material Science, Queen Mary University of London, London, U.K.*
[3]*School of Electrical Engineering, VIT University, Chennai, India*

(Received December 12, 2018, Revised May 7, 2019, Accepted May 10, 2019)

Abstract. Flow through a scaled horizontal axis marine current turbine was numerically simulated after validation and the turbine design was optimized. The computational fluid dynamics (CFD) code Ansys-CFX 16.1 for numerical modeling, an in-house blade element momentum (BEM) code for analytical modeling and an in-house surrogate-based optimization (SBO) code were used to find an optimal turbine design. The blade-pitch angle (θ) and the number of rotor blades (NR) were taken as design variables. A single objective optimization approach was utilized in the present work. The defined objective function was the turbine's power coefficient (C_P). A 3x3 full-factorial sampling technique was used to define the sample space. This sampling technique gave different turbine designs, which were further evaluated for the objective function by solving the Reynolds-Averaged Navier–Stokes equations (RANS). Finally, the SBO technique with search algorithm produced an optimal design. It is found that the optimal design has improved the objective function by 26.5%. This article presents the solution approach, analysis of the turbine flow field and the predictability of various surrogate based techniques.

Keywords: marine current turbine; CFD; BEM; single objective optimization; surrogate modeling

1. Introduction

Marine current energy began to draw global attention during the 1970s. Marine current turbine (MCT) have several design variations to harvest such energy (Bahaj and Myers 2003) and classification is shown in Fig. 1. An axial flow MCT results in higher power coefficient (C_P) owing to the fact that each and every blade contribute to the power output. However, MCT needs design optimization studies to improve overall performance. Early stage experiments were conducted for a 0.8 m MCT and performance characteristics were captured (Myers and Bahaj 2007). Numerical and experimental investigations to design a hydro spinnal turbine resulted low C_P values (Rosli *et al*. 2016). According to the Betz limit, the maximum value attainable by a turbine is C_P=0.593, while a modified MCT design fixed in a waterway can cross Betz limit (Vennell 2013).

*Corresponding author, Associate Professor, E-mail: samad@iitm.ac.in

http://www.techno-press.org/?journal=ose&subpage=7 ISSN: 2093-6702 (Print), 2093-677X (Online)

RANS equations were solved for an actuator disk kept in water as a preliminary analysis (Nishino and Willden 2012). A 0.4 m horizontal axis MCT was numerically studied to predict the performance and identify the effects of cavitation (Bal *et al.* 2015). The change in number of rotor blades (*NR*) and blade-pitch angle (θ) alters the lift-to-drag ratio. A notable reduction in overall drag can be seen while incorporating positive blade-pitch angle and fewer number of blades (Amet *et al.* 2009). Blade twist angle (*ß*) in MCT leads to effortless self-starting which is advantageous in using twisted blades. It is also found that modifications in *NR* and θ have increased the turbine's C_P (Chini *et al*. 2011). Blockage ratio, solidity, and chord length were also considered to improve the performance (Priegue and Stoesser 2016, Schluntz and Willden 2015, Subhra Mukherji *et al*. 2011). Table 1 highlights different parameters, turbine diameter, methods chosen and performance achieved by various authors

There are several optimization approaches and in many cases surrogates assists in reducing computational costs. Table 2 shows various authors using different parameter and methods to improve the objective functions. A single surrogate may not predict an efficient optimal point using the optimizer and thus different surrogates are considered. The efficiency of the surrogates depends on the nature of the problem. Thus the applicability of the surrogates needs to be evaluated for individual problem (Samad *et al.* 2008).

The current work deals with the selection of parameters (*NR* & θ) and the MCT optimization through various surrogate methods. Methodologies like BEM and CFD analysis incorporated with surrogate techniques are also presented. The performance and fluid flow behavior are discussed.

Table 1 Parametric study of horizontal axis MCT

Authors	Turbine	Parameter	Method/Model	Performance
(Bahaj *et al.* 2007)	*D*=0.8 m, *NR*=3	θ	Lab test	C_P = 0.45
(Batten *et al.* 2007)	*D*=0.8 m, *NR*=3	θ	BEM	C_P = 0.45
(Liu *et al*. 2017)	*D*=1 m, *NR*=3	ß & nacelle shape	BEM & CFD - Realizable *k*-ε	Thrust increased by 7.8%
(Barber 2017)	*D*=20 m, *NR*=2	θ	BEM	C_P = 0.48
(Zhu *et al.* 2017)	*D*=0.8 m, *NR*=3	θ & winglet	CFD – Spalart Allmaras	C_P = 0.51
(Ren *et al.* 2017)	*D*=0.8 m, *NR*=3	Winglet	CFD - *k*-ω SST	C_P = 0.425
(Wei *et al.* 2015)	*D*=20 m, *NR*=3&5	θ & D_a	Lab test & BEM	C_P = 0.44
(Schleicher *et al*. 2015)	*D*=0.53 m	*NR*	CFD - *k*-ω SST	C_P = 0.43
(Tian *et al.* 2016b)	*D*=3 m, *NR*=3	Yaw angle	CFD - *k*-ω SST	C_P = 0.46
(Goundar *et al.* 2012)	*D*=10 m, *NR*=3	θ & *NR*	Lab test	C_P = 0.47
(Morris *et al.* 2016)	*D*=10 m, *NR*=3	*NR*	CFD - *k*-ω SST	C_P = 0.46

Table 2 Study on MCT optimization

Author	Parameter	Method	Objective	Performance
(Kolekar and Banerjee 2013)	c & β	GA	Maximize C_P	C_P increased by 17%
(Coiro *et al*. 2016)	θ & diffuser	GA	Maximize C_P	C_P increased by 6.1%
(Huang and Kanemoto 2015)	θ & NR	GA	Maximize C_P	C_P = 0.425
(Zhu *et al*. 2012)	θ	NSGA II	Maximize C_P, Maximize C_T	C_P = 0.34
(Tahani *et al*. 2015)	c & β	GA	Maximize C_P	C_P = 0.486

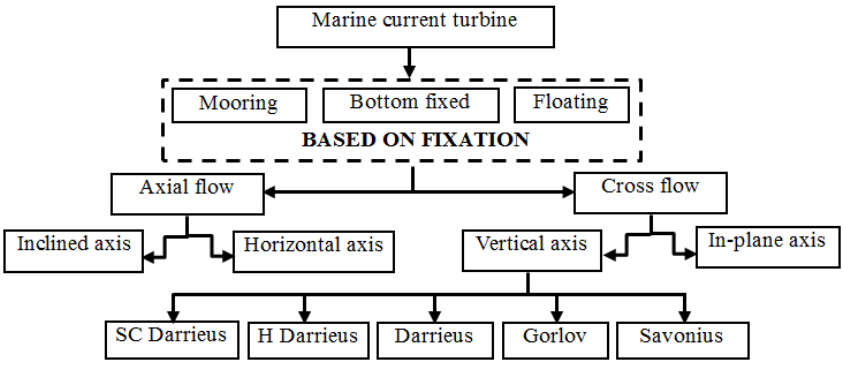

Fig. 1 Current turbine classification

2. Numerical methodology

A three-blade horizontal axis MCT with pitch angle θ=25^o was numerically simulated using CFD and BEM codes. The tip diameter and hub diameter are 0.8 and 0.1 m respectively. Rotor blades are formed from 63-812, 63-815, 63-818, 63-821 and 638-24 NACA profiles series for 17 stations along the blade (Batten *et al*. 2007, Blackmore *et al*. 2016) which is given in Table 3.

2.1 Blade element momentum theory

The BEM method used for the current study is taken from the work of Glauert (Hansen 2015) and coded in FORTRAN. The rotor is modeled as an infinitesimally thin porous disk having a continuous velocity. Both velocity and pressure are taken as radially dependent but not azimuthally-dependent in the steady BEM approach. The rotational effect of the blades is modeled through tangential and axial induction factors (a', a)

$$u(r) = U_T[1 - a(r)] \ , \ v = \Omega r \ [1 + a(r)'] \tag{1}$$

Table 3 Turbine blade profile data

r/R	R	c/R	θ	t/c
0.20	0.08	0.1250	15.0	24.0
0.25	0.10	0.1203	12.1	22.5
0.30	0.12	0.1156	9.5	20.7
0.35	0.14	0.1109	7.6	19.5
0.40	0.16	0.1063	6.1	18.7
0.45	0.18	0.1016	4.9	18.1
0.50	0.20	0.0969	3.9	17.6
0.55	0.22	0.0922	3.1	17.1
0.60	0.24	0.0875	2.4	16.6
0.65	0.26	0.0828	1.9	16.1
0.70	0.28	0.0781	1.5	15.6
0.75	0.30	0.0734	1.2	15.1
0.80	0.32	0.0688	0.9	14.6
0.85	0.34	0.0641	0.6	14.1
0.90	0.36	0.0594	0.4	13.6
0.95	0.38	0.0547	0.2	13.1
1.00	0.40	0.0500	0	12.6

where, u denotes axial velocity and v is the tangential velocity at the disk. The disk is divided to radial rings where arguments based on the integral continuity and momentum equations find the thrust and torque. The thrust denotes the axial force acting in the direction of the incoming flow. The BEM method also finds the thrust and torque that acts on the blade radial elements, assuming to know the angle of attack variations with the profile's C_L and C_D. Thrust and torque expressions from the momentum and blade element methods are the same and provides non-linear equations for a and a' for each of the radial elements. The equations are solved using a linear iterative solver. Once a and a' are known, the torque and the thrust for each radial element is calculated and then radially integrated to yield the overall thrust and power. Prandtl's and Goldstein's tip and hub loss factors have also been incorporated. At a post-stall condition, the C_L and C_D were calculated using the empirical relations of Viterna and Janetzke (Moriarty and Hansen 2005). Snel's model was used to account for the delay effect of the rotation on the stall. The code used in this study has already been successfully used in its steady and unsteady versions for MCT (Ai *et al.* 2016).

2.2 Computational fluid dynamics

A 3D periodic single blade passage CAD model (Fig. 2) was implemented to reduce the CFD simulation time (Karthikeyan *et al.* 2017). The periodic domain had refined mesh near the blade and hub. The periodic boundary surfaces measures 120^o for the turbine with 3 blades (NR=3). Similarly, the angles were 180^o and 90^o for NR=2 and 4, respectively. To resolve the strong

transverse gradients within the boundary layer, 18 inflated prism layers with unstructured tetrahedron mesh were created (Fig. 3). The cell growth ratio was maintained at 1.1 throughout the boundary layer thickness to minimize numerical diffusions. The RANS equations represent the time-averaged continuity and momentum equations that govern the fluid flow. For a steady incompressible flow, the equations are

$$\nabla \cdot u_i = 0 \tag{2}$$

$$\rho \frac{\partial}{\partial x_j}(u_i u_j) = \frac{\partial}{\partial x_j}\left[-p\delta_{ij} + \mu\left(\frac{\partial u_i}{\partial x_j} + \frac{\partial u_j}{\partial x_i}\right)\right] + \rho \frac{\partial}{\partial x_j}(-\overline{u_i' u_j'}) \tag{3}$$

The grid independent test (Fig. 4) shows that the difference in C_P values between 10 million and 13 million tetrahedrons was insignificant. Hence 10 million tetrahedron elements were chosen for further simulations. RANS equation with *k-ω* SST turbulence closure model (Menter 1994) is chosen and $y^+ =\sim 1$ was maintained.

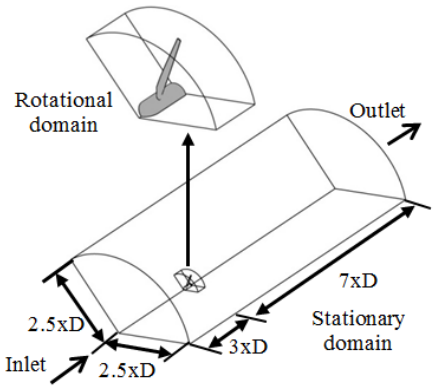

Fig. 2 Fluid domain extraction

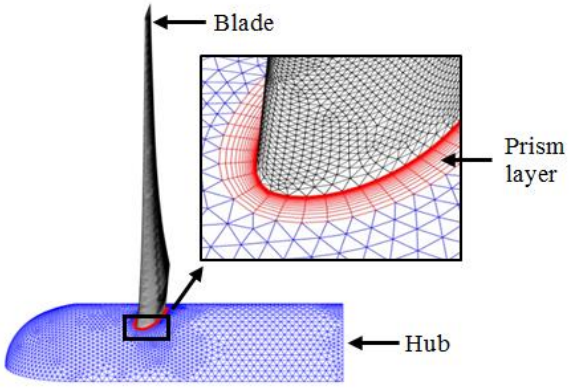

Fig. 3 Mesh with inflated prism layers

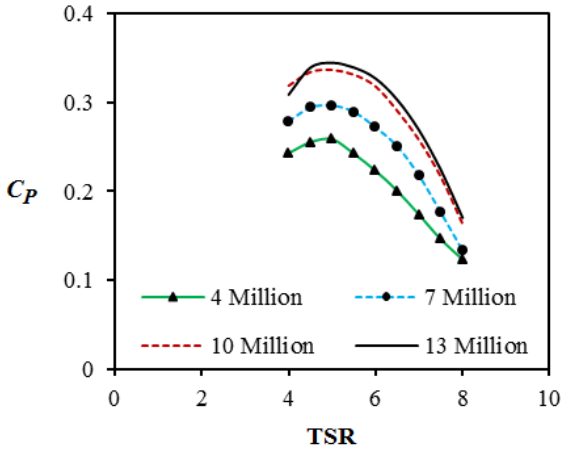

Fig. 4 Grid independent study

Table 4 Boundary conditions

Parameter	Description
Fluid flow domain	Single blade
Number of elements	10 million
Mesh type	Hybrid
Fluid medium	Water
Turbulence model	*K-ω* SST
Inlet condition	Velocity inlet
Outlet condition	Pressure outlet
Residual convergence value	$1x10^{-5}$
Mass imbalance	0.00001

The high-resolution advection scheme was used for better accuracy. Table 4 has the details about boundary conditions, convergence criterion for the velocity and pressure components and mass imbalance. IBM iDataPlex dx360 M4 high-performance computing (Virgo) facility, which is available at Indian Institute of Technology Madras, was used for simulation. A single simulation takes around 50 hours. The performance of the MCT is governed by the tip speed ratio (TSR) (Bai *et al.* 2014) and the performance is identified by the C_P.

$$\text{Tip speed ratio:} \qquad \text{TSR} = \frac{\Omega R}{U_T} \tag{4}$$

$$\text{Power coefficient:} \qquad c_P = \frac{Q\Omega}{0.5\rho\pi R^2 U_T^3} \tag{5}$$

3. Numerical optimization

The initial optimization process involves selecting design variables, objective function and setting the design space. Later, it involves identifying the sample points and solving in CFD to find the optimal point (Fig. 5). The two variables, the objective function (C_P) were selected and a three-level full-factorial sampling scheme was utilized. This sampling scheme gave 9 different design points containing all possible combinations which were used for CFD analysis. The results from the CFD code were fed as input data for the surrogate models to predict the optimal design. The problem dependent surrogates cannot generate the initial data and depend on high fidelity CFD results.

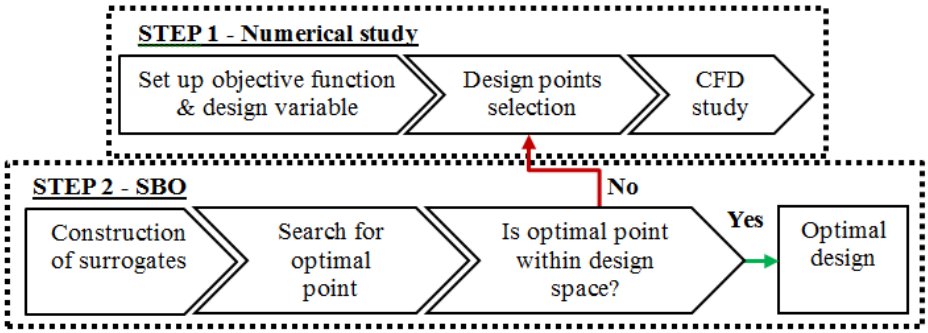

Fig. 5 Methodology for optimization

Table 5 Design space for optimization

Variable	Lower	Upper
θ	15^o	25^o
NR	2	4

Table 6 Design points

S.N	θ	*NR*
1	15^o	2
2	15^o	3
3	15^o	4
4	20^o	2
5	20^o	3
6	20^o	4
7	25^o	2
8	25^o	3
9	25^o	4

Multiple surrogates produce different optimal points using the same set of initial data (Badhurshah and Samad 2015). This finds a better alternative and increases the robustness of surrogates. Finally, a search algorithm identifies optimal points from the surrogates (Koo *et al*. 2014).

The upper, lower limit for variable 1 (θ) was chosen and found to be that θ>25$^{\mathbf{o}}$ or <15$^{\mathbf{o}}$ is inefficient (Bahaj *et al*. 2007). The design space and design points are shown in Tables 5 and 6.

3.1 Response surface approximation model (RSA)

It is an assortment of a mathematical and statistical approach to build an empirical model (Ezhilsabareesh *et al.* 2018). It has been used in the field of turbomachinery optimzation to fit the objective function using minimal sample points. Response surface approximation (RSA) model evaluates the response using a second order polynomial fit and the same is expressed as

$$F = \beta_0 + \sum_{j=1}^{n} \beta_j X_j + \sum_{j=1}^{n} \beta_{jj} X_j^2 + \sum_i \sum_{j>i}^{n} \beta_{ij} X_i X_j \quad (6)$$

Here, $X's$ and *n* denotes design variables and number of design variables. $\beta's$ are the regression coefficients obtained by least square regression.

3.2 Radial basis function (RBF)

It performs a nonlinear transformation of input vectors using a Gaussian function (ψ) as an activation function. It has a linear output layer with hidden and output layer (Gong *et al.* 2016). A real-valued function produce for each input vectors, and radial basis neurons are fed to the linear output layer to produce the output(Ezhilsabareesh *et al*. 2018, Samad *et al*. 2008). *X* is design point, *t* represents sample point, w_0 is weight coefficient and w_i is the bias term. The approximation produced by RBF is expressed as

$$y(x) = w_0 + \sum_{i=1}^{N} w_i \psi(X - t) \quad (7)$$

3.3 Kriging model

Kriging (KRG) is based on interpolation. KRG is defined as the sum of deviation and mean terms (Lee *et al*. 2016). The KRG model estimates the unknown function as a combination of two parts; a stable global model of design space *g*(*x*) for capturing large scale variation and small scale variations are captured by $Z(x)$. KRG is a consolidation of global model and departures (Samad *et al*. 2008) of the following form

$$y(x) = g(x) + Z(x) \quad (8)$$

The predicted residual error sum of squares (PRESS) is a form of cross-validation that provides a measure of fit. Weights are determined based on the error. The surrogates with high error contribute to low weight. In the present work, the global weights are chosen by PRESS or leave-one-out cross-validation, which is a global data-based measure of goodness. The weights are estimated and are calculated as

$$w_i = w_i^* / \sum_i w_i^* \quad (9)$$

$$E_{avg} = \frac{1}{N}\sum_{i=1}^{N} E_i \tag{10}$$

$$w_i^* = (E_i/E_{avg} + \alpha)^{\gamma} \tag{11}$$

E_i and N are the errors from the PRESS and the number of surrogates. The parameter α=0.05 and γ=-1 are determined analytically and reported (Goel *et al.* 2007). The same were used in the present work. Sequential quadratic programming (SQP) is the local search method which is incorporated to acquire optimal points. The SQP uses initial guess values to find an optimal point.

4. Results and discussion

A constant U_T =1.54 m/s is used for simulations and the results are compared with experiments (Batten *et al.* 2007). The 2D BEM results have a closer value to the experimental data in Fig. 6. BEM is unable to introduce swirling action into the flow, thus the turbulence effects are neglected while predicting the C_P (Batten *et al.* 2013, Turnock *et al*. 2011). The 3D effect of a finite number of blades and its rotational effects introduce complex flow which comprises fluid model separation, stall, blade tip vortex and all these cannot be predicted by the BEM. The BEM is based on numerical C_L, C_D and generally overestimates power extraction (Guo *et al*. 2015). Thus BEM results closely matches with the experiment. The CFD results include all the losses caused which reduce the C_P values and follows a similar trend to experimental data. Moreover, several authors have proven that the CFD values fall below the experimental values while using RANS and commercial tools (Kinnas *et al.* 2012, Leroux *et al*. 2019; Rahimian *et al.* 2018, Tian *et al.* 2016a). The experimental uncertainties which were around 2% (Bahaj *et al.* 2007), could also lead to deviation between experimental and CFD results.

The *k-ω* SST turbulence model performs better than the *k-ε* model with a deviation of 8.04%. The high-resolution advection scheme was used for better accuracy. The experimental and the CFD results produce $C_{P(Peak)}$=0.375 and 0.346, respectively.

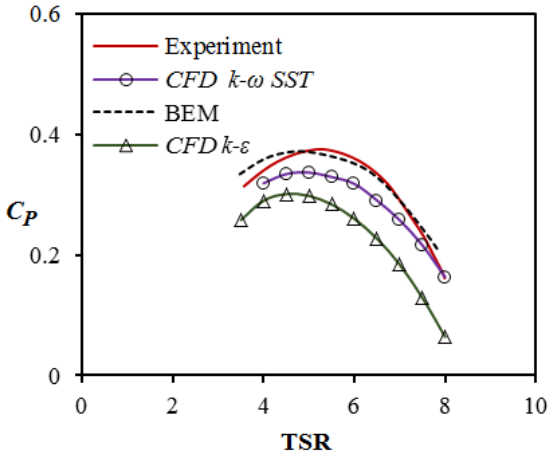

Fig. 6 CFD and BEM Validation curve for TREF (θ=25° and NR=3)

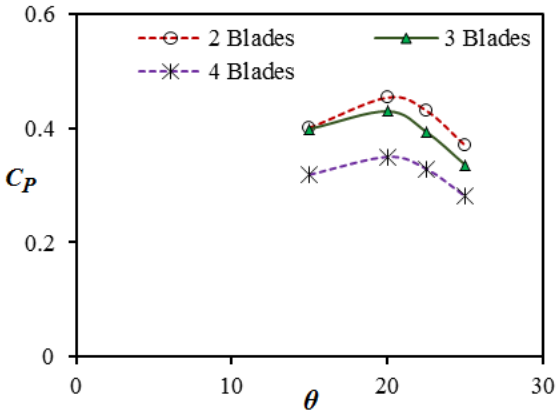

Fig. 7 CFD curves for different θ and N_R

The turbine with NR=4 and θ=20° has a $C_{P(Peak)}$=0.351. While, NR=2 and θ=20° gave $C_{P(Peak)}$=0.454, which is a significant increase in $C_{P(Peak)}$. Fig. 7 shows that θ=20° produces high C_P for NR=2 to 4 at TSR=5.5. The turbine with NR=3 and θ=20° has a $C_{P(Peak)}$=0.43. The overall drag increases as NR increases (Delafin *et al*. 2016) and thus the turbine with NR=4 yields low C_P. RBF gives a high PRESS and lower weight which is tabulated in Table 7. RSA and KRG gave low PRESS and high weights.

Table 7 PRESS and weights

Model	PRESS	Weights
RBF	0.115	0.226
RSA	0.046	0.389
KRG	0.048	0.383

Table 8 Design optimization results

Model	θ	NR	F_{SUR}	F_{CFD}	F_{ERR}
RBF	17.48°	2	0.630	0.542	0.139
RSA	18.29°	2	0.561	0.535	0.046
KRG	19.47°	2	0.566	0.543	0.042

Table 9 BEM results

θ	NR	$C_{P(Peak)}$
19.47°	2	0.391
19.47°	3	0.401
19.47°	4	0.370

Table 8 shows the surrogates predicted objective function values. KRG yields C_P=0.566, for NR=2 and θ=19.47°. KRG predicted design was simulated and it was found that the error in C_P between the surrogate and CFD (F_{ERR}) is 0.042, which is the lowest of all the surrogates. The design point is fed into the BEM code to further evaluate the objective function. The $C_{P(peak)}$ for θ=19.47° and NR=2 to 4 was evaluated using the BEM code. The BEM result from Table 9 confirms that NR=4 has the lowest $C_{P(Peak)}$ which is similar to the CFD results. The performance between TREF and TOPT were compared for the complete working range in Fig. 8. The maximum C_P value of TREF is close to TSR=5.5. The change in θ from 15° to 30° has been reported and the optimal TSR changes from 4.8 to 6 respectively (Bahaj *et al*. 2007). Even a small change in θ leads to change in C_L values of the MCT. Also, the change in NR will lead to a shift in optimal TSR value and the working range of the MCT. The TOPT works effectively between TSR=5 to 8.

Table 10 compares the power output that can be produced by the TREF and TOPT. TREF produced a $P_{out(peak)}$=343.84 W, whereas TOPT produced 497.85 W. However, the U_T could typically vary from 0.5 to 2 m/s in real sea condition. Thus it is important for the TOPT to work effectively in this range. To examine the same, CFD simulations of TOPT were carried on for U_T=0.5, 1 and 2 m/s. Fig. 9 compares the C_P vs. TSR for U_T=0.5, 1, 1.54 and 2 m/s. The C_P achieved by U_T=0.5 m/s is low for the complete working range due to its low corresponding torque. U_T=2 m/s has achieved high C_P values. However, there is minimal difference between U_T=1.54 and 2 m/s. This convinced that TOPT is optimal for the varying U_T.

The pressure coefficient (C_{PR}) contours for the TREF and TOPT are compared in Fig. 10. The C_{PR} on MCT blade varies from hub to tip. The gradual change on local θ from hub to tip causes a difference in pressure and alters the C_L and C_D characteristics. The C_{PR} at the suction side (SS) is relatively lower near the tip of TOPT than TREF. It also states that the fluid velocity varies gradually from hub to tip in TOPT.

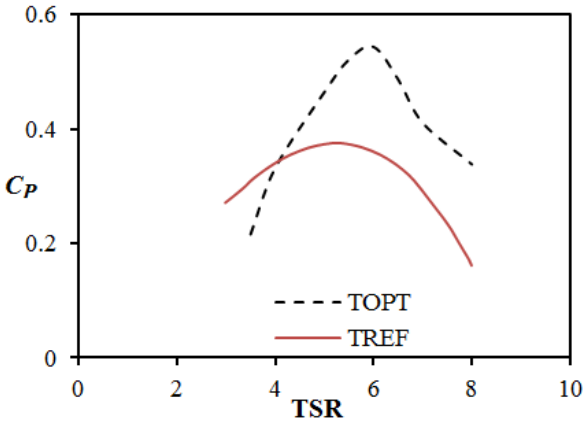

Fig. 8 Comparison of TREF and TOPT

Table 10 CFD results

Design	θ	NR	$P_{out(Peak)}$
T_{REF}	25°	3	343.84 W
T_{OPT}	19.47°	2	497.85 W

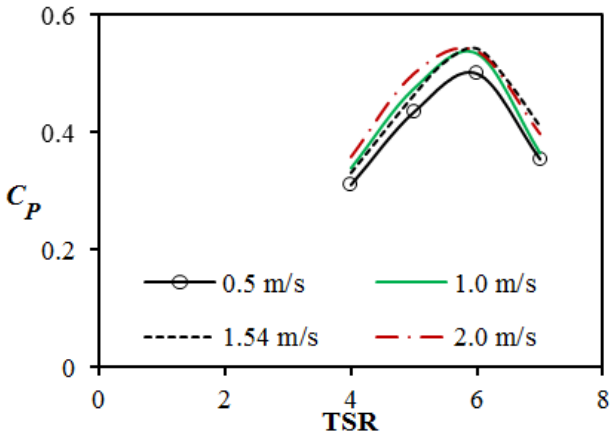

Fig. 9 Different free stream velocities comparison (TOPT)

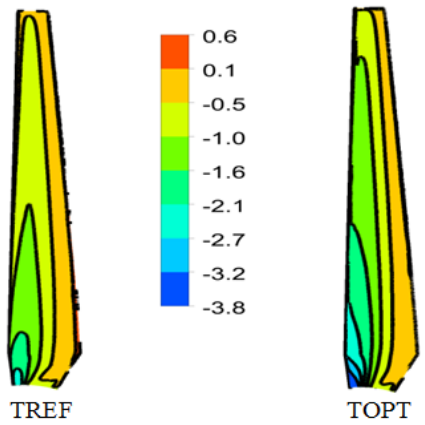

Fig. 10 Pressure coefficient contour on MCT

Fig. 11 compares the blade loading between TREF and TOPT at three different location (x/c = 0.25, 0.5, 0.75). The area circumscribed by the C_{PR} curves determines the blade loading that delivers the work on MCT shaft. A better blade loading can be noticed for the optimized turbine in all three locations. TREF's C_{PR} vs. x/c curve is different from TOPT which experiences reduced pressure values at SS. This shows that high fluid velocity is achieved at SS of the blade. The region of the adverse pressure gradient is shifted in TOPT. The PS $C_{PR(\max)}$ values are similar for TREF and TOPT, however, the SS values are varying. The TOPT has a lower C_{PR} value at the SS trailing edge (TE) due to its change in θ near the blade tip.

Fig. 12 compares the MCT's non-dimensional velocity variation from the root to the tip. A higher blade velocity is seen in TOPT due to a gradual change in local θ. Also, the change in θ delayed the fluid separation from the blade which is advantageous. The streamlines given in Fig. 12 is evident to state the early separation of fluid from the blade in TREF. The early separation

happens at the root till r/R=0.8 which causes high drag and downstream wake. This decreases the overall performance of TREF.

Fig. 13 shows the fluid velocity near the blade tip (r/R=0.99) comparing the normalized average velocity of TREF and TOPT. The blade tip reaches high fluid velocity at TSR=4, 6 and 8 for TOPT at SS. A low-velocity region at the pressure side (PS) of the TOPT was also noticed. Unlike TOPT, TREF has a different velocity contour. TREF creates high fluid velocity in the PS which affects the pressure acting on the blade to create lift. This is an unfavorable condition for the MCT.

The 3D streamlines in Fig. 14 shows a helicoidal shape due to the rotational velocity of the turbine. The increase in *NR* on TREF intervenes the fluid passing by and converts some energy of incoming free stream to swirls. The wake recovery delays in TREF and affects the performance of the turbine. Fig. 15 shows the surface streamline of TREF and TOPT at r/R=0.1, 0.5, 0.9. A wider fluid recirculation region at r/R=0.1was noticed. The vortices formed near the root of the blade are diminished near the tip.

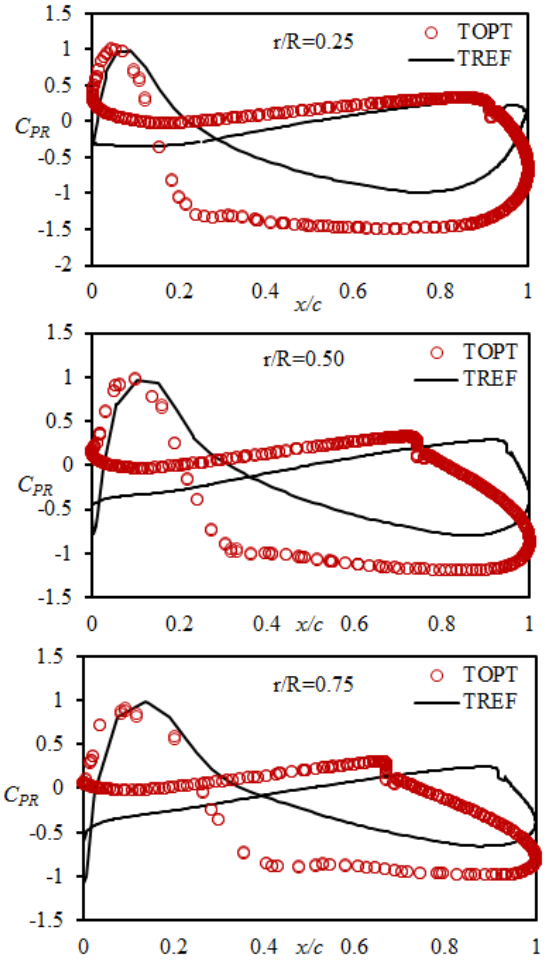

Fig. 11 Blade loading curve comparison between TREF and TOPT

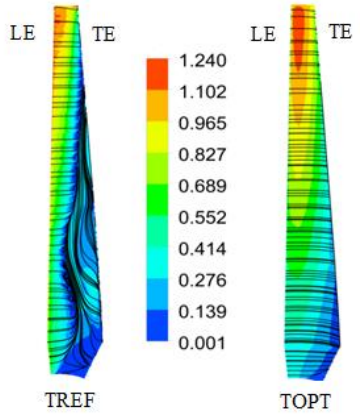

Fig. 12 Surface streamlines on blade SS with velocity contours

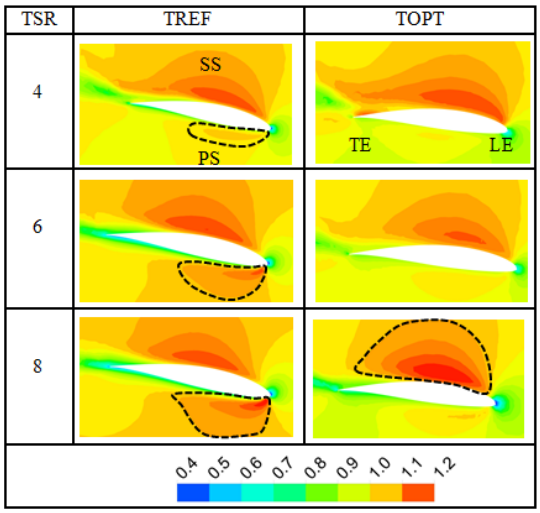

Fig. 13 Normalized average velocity contours of different TSR at r/R=0.99

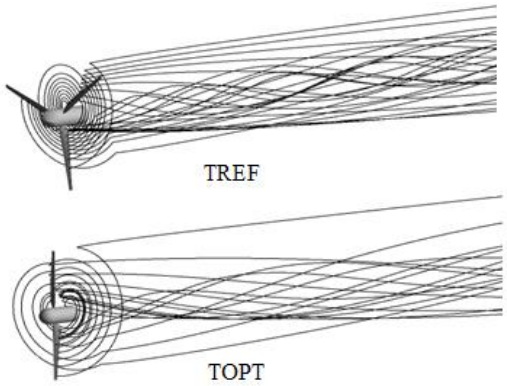

Fig. 14 3D Streamlines comparison

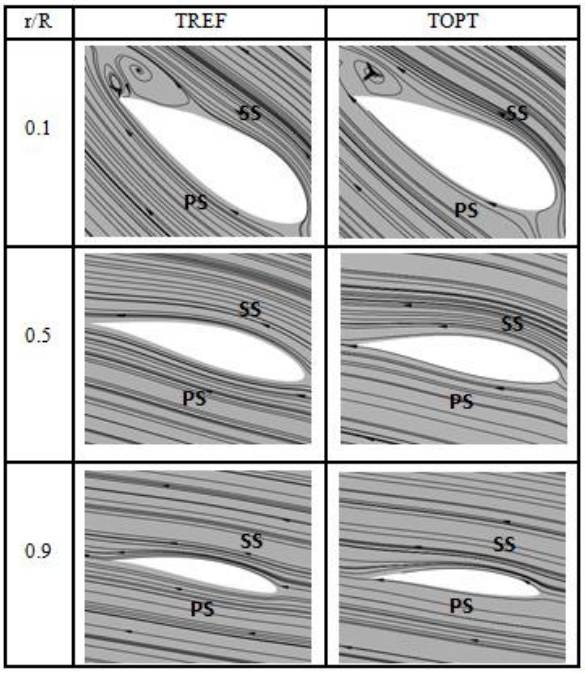

Fig. 15 Surface streamlines for TSR=6

Fig. 16 compares the surface streamlines for both TREF and TOPT at r/R= 0.1. A wider fluid recirculation region was noticed on the TREF. The fluid recirculates in both clockwise and anticlockwise directions near the TE. The counter-rotating vortices were formed at the TREF at TSR=4 which experiences high variations in pressure gradients. The region of counter-rotating vortices was gradually reduced at TSR=8 due to the increased fluid velocity. The change in θ from 25^{o} to 19.5^{o} has reduced the incidence angle and the sudden pressure variations which avoided counter-rotating vortices in TOPT. Thus TOPT was noticed with a comparatively smaller fluid recirculation at the SS. In TOPT, a smaller recirculation region was noticed and there is a delay in the fluid separation irrespective to any TSR.

Fig. 17 compares the non-dimensional axial velocity of TREF and TOPT. The axial velocity decreases at the downstream of TREF and a larger region of axial deficit can be noted. The low-velocity region is significantly reduced in TOPT. This is due to the mixing of fluid at the downstream of the turbine. The vortex cores at SS and PS is larger at the tip of TREF than TOPT (Fig. 18). The TE of TREF produces an additional vortex which is wider at SS and PS. The change in θ reduces vortex at the TOPT LE. The TREF PS has a larger vortex core region.

Fig. 19 compares the streamwise vorticity of the TREF and TOPT. The tips of the blades are highlighted to discuss the tip vortex. The strength of counter-rotating pairs is high and unstable near the tip in TREF. This channels a way for tip leakage losses in TREF which is due to the change in local θ at the blade tip. The mass flow that escapes through the tip of TREF causes loss in power production. A weaker vortex is seen in TOPT which is bound to faster dissipation.

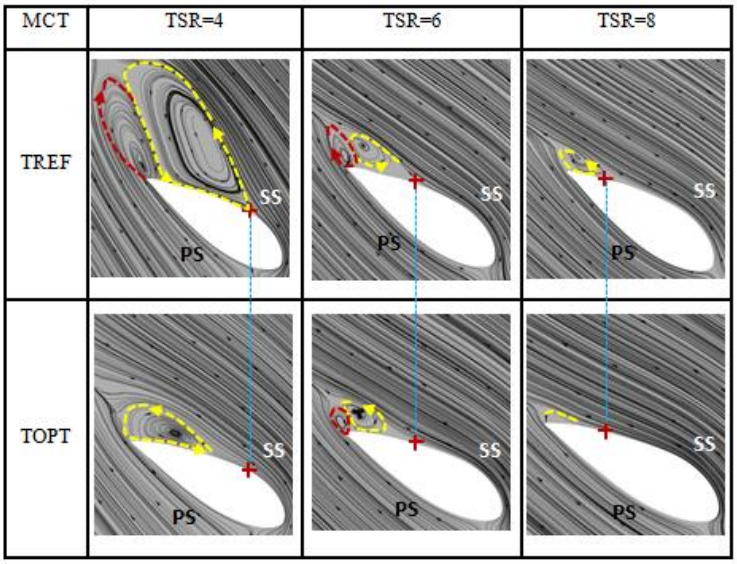

Fig. 16 Surface streamlines at r/R=0.1

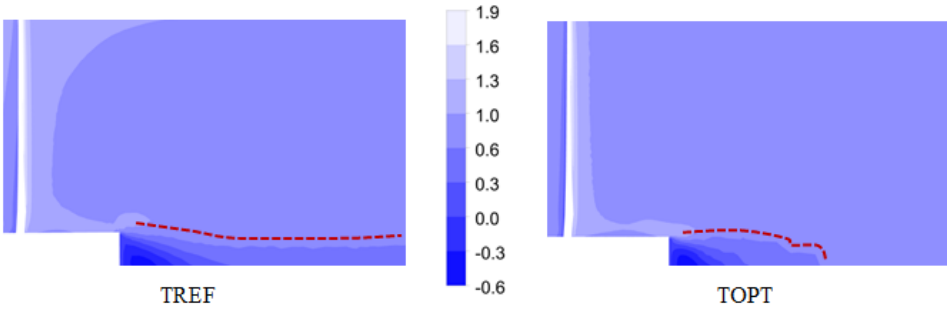

Fig. 17 Axial velocity contours at the downstream of MCT

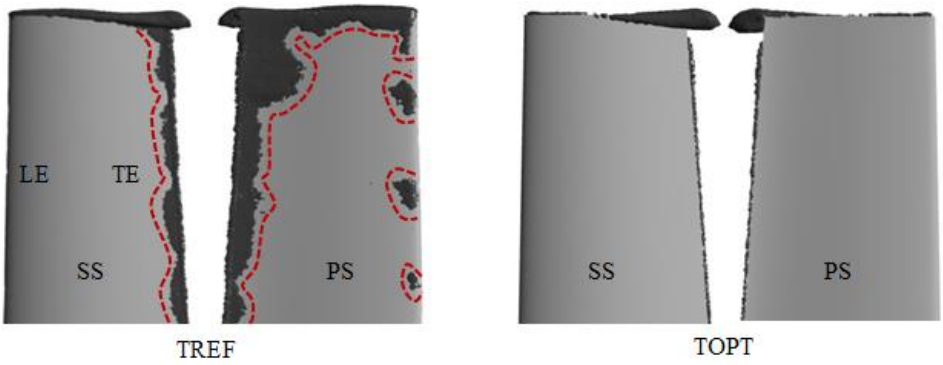

Fig. 18 Vortex core region comparison

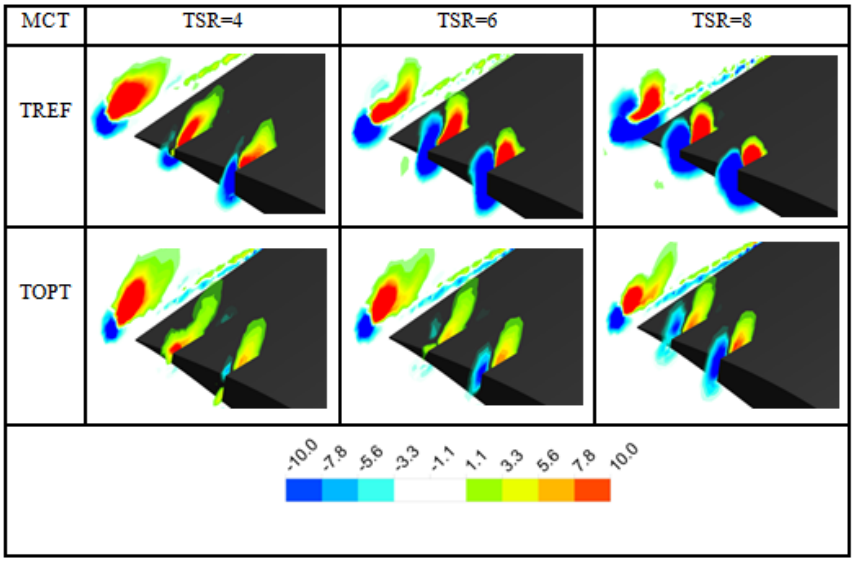

Fig. 19 Streamwise vorticity comparison

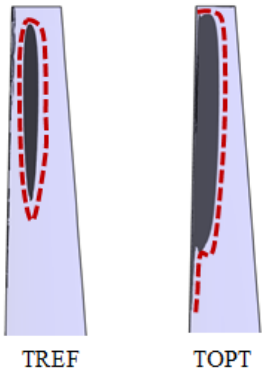

Fig. 20 Cavitation ratio comparison

Finally, it is important to understand that the cavitation inception of TREF and TOPT. The ratio of critical cavitation ($\sigma_{Critical}$) and local cavitation (σ_{Local}) is the cavitation ratio (σ^*). It is found that $\sigma^*<1$ faces cavitation. It was observed that the cavitation on TREF is 15% of the total blade span if TSR>8. While using the AeroDyn model, it was predicted to increase by 2 to 9% (Murray 2017). Hence calculating σ^* at TSR>8 shows the extreme possibility of cavitation at the blade tip.

Fig. 20 shows the $\sigma^*=0.7$, however, $\sigma^*= 0.99$ to 0.79 did not face any cavitation. The region of cavitation has slightly increased in TOPT and it can be reduced if fouling and angular velocity are chosen correctly. The cavitation at the blade tip can also be reduced by introducing serrated tips. The design point used in the present study does not face cavitation inception which keeps TOPT safe from cavitation. All these fluid phenomena have contributed TOPT to achieve higher C_P

values. The reduction in the number of rotor blades on TOPT reduces the material cost and MCT becomes lighter, which is advantageous to operate at a lower U_T.

5. Conclusions

For the design optimization of a marine current turbine (MCT) with CFD, blade element momentum theory and surrogate-based optimization are reported. The power coefficient (C_P) was improved by adjusting the blade-pitch angle (θ) and the number of blades (NR). The conclusions are:

- The optimized MCT has a lesser number of rotor blades (NR=2) and the blade-pitch angle is reduced from θ=25º to 19.5º. The blade-pitch angle was more sensitive in altering the turbine's C_P.
- Vortex cores and recirculation regions were reduced in the optimized turbine due to the change in the angle of incidence. The optimized turbine gave a maximum C_P=0.543 at TSR=6.
- The CFD results of the MCT with θ =20º and NR=3 achieved a maximum C_P=0.43, However, the optimized turbine has a further 26.5% increase in C_P.
- The power produced by the optimized turbine is 154.01 W higher than the reference turbine and is capable of working in a varying free stream velocity (U_T=0.5 to 2 m/s).
- Increase in power coefficient can increase the region of cavitation inception in TOPT if TSR exceeds the design TSR.
- Kriging was the chosen surrogate due to its low error (F_{ERR}=0.042). The multiple surrogates help to predict and improve the MCT performance.

Acknowledgments

The authors acknowledge the support of the UK India Education and Research Initiative (UKIERE) and Department of Science & Technology (DST), India. (No. UKIERI-DST-2014-15-066).

References

Aerodyn, V. and Murray, R. (2017), Predicting Cavitation on Marine and Hydrokinetic Turbine Predicting Cavitation on Marine and Hydrokinetic Turbine Blades with AeroDyn V15.04.Technical report, NREL /TP-5000-68398, August 2017.

Ai, K., Avital, E.J., Korakianitis, T., Samad, A., Venkatesan, N., Eng, O., *et al*. (2016), "Surface wave effect on marine current turbine, modelling and analysis", *Proceedings of the 7th International Conference on Mechanical and Aerospace Engineerng, UK*.

Amet, E., Maître, T., Pellone, C. and Achard, J.L. (2009), "2D numerical simulations of blade-vortex interaction in a darrieus turbine", *J. Fluid. Eng. T- ASME*, **131**, 111103. doi:10.1115/1.4000258.

Badhurshah, R. and Samad, A. (2015), "Multiple surrogate based optimization of a bidirectional impulse turbine for wave energy conversion", *Renew. Energ.*, **74**, 749-760. doi:10.1016/j.renene.2014.09.001.

Bahaj, A.S., Molland, A.F., Chaplin, J.R. and Batten, W.M.J. (2007), "Power and thrust measurements of marine current turbines under various hydrodynamic flow conditions in a cavitation tunnel and a towing tank", *Renew. Energ.*, **32**, 407-426. doi:10.1016/j.renene.2006.01.012.

Bahaj, A.S. and Myers, L.E. (2003), "Fundamentals applicable to the utilisation of marine current turbines for energy production", *Renew. Energ.*, **28**, 2205-2211. doi:10.1016/S0960-1481(03)00103-4.

Bai, X., Avital, E.J., Munjiza, A. and Williams, J.J.R. (2014), "Numerical simulation of a marine current turbine in free surface flow", *Renew. Energ.*, **63**, 715-723. doi:10.1016/j.renene.2013.09.042.

Bal, S., Atlar, M. and Usar, D. (2015), "Performance prediction of horizontal axis marine current turbines", *Ocean Syst. Eng.*, **5**(2), 125-138. doi:10.12989/ose.2015.5.2.125.

Barber, R.B. (2017), Adaptive Pitch Composite Blades for Axial-Flow Marine Hydrokinetic Turbines.

Batten, W.M.J., Bahaj, A.S., Molland, A.F. and Chaplin, J.R. (2007), "Experimentally validated numerical method for the hydrodynamic design of horizontal axis tidal turbines", *Ocean Eng.*, **34**, 1013-1020. doi:10.1016/j.oceaneng.2006.04.008.

Batten, W.M.J., Harrison, M.E. and Bahaj, A.S. (2013), "Accuracy of the actuator disc-RANS approach for predicting the performance and wake of tidal turbines", *Philos. Trans. A. Math. Phys. Eng. Sci.*, **371**, 20120293. doi:10.1098/rsta.2012.0293.

Blackmore, T., Myers, L.E. and Bahaj, A.S. (2016), "Effects of turbulence on tidal turbines: Implications to performance, blade loads, and condition monitoring", *Int. J. Mar. Energy*, **14**, 1-26. doi:10.1016/j.ijome.2016.04.017.

Chini, R., Ordonez, M. and Bachmayer, R. (2011), "Blades optimization for an ocean current horizontal axis turbine using response surface methodology", *Ocean. 2011 IEEE - Spain*. doi:10.1109/Oceans-Spain.2011.6003646.

Coiro, D.P., Daniele, E. and Della Vecchia, P. (2016), "Diffuser shape optimization for GEM, a tethered system based on two horizontal axis hydro turbines", *Int. J. Mar. Energy*, **13**, 169-179. doi:10.1016/j.ijome.2015.08.002.

Delafin, P., Nishino, T., Wang, L. and Kolios, A. (2016), "Effect of the number of blades and solidity on the performance of a vertical axis wind turbine", *J. Phys. Conf. Ser.*, **753**, 022033. doi:10.1088/1742-6596/753/2/022033.

Ezhilsabareesh, K., Rhee, S.H. and Samad, A. (2018), "Shape optimization of a bidirectional impulse turbine via surrogate models", *Eng. Appl. Comput. Fluid Mech.*, **12**, 1-12. doi:10.1080/19942060.2017.1330709.

Goel, T., Haftka, R.T., Shyy, W. and Queipo, N.V. (2007), "Ensemble of surrogates", 199-216. doi:10.1007/s00158-006-0051-9.

Gong, X., Liao, D., Chen, T., Zhou, J. and Yin, Y. (2016), "Optimization of steel casting feeding system based on BP neural network and genetic algorithm", *China Foundry*, **13**(3), 182-190. doi:10.1007/s41230-016-6008-8.

Goundar, J.N., Ahmed, M.R. and Lee, Y.H. (2012), "Numerical and experimental studies on hydrofoils for marine current turbines", *Renew. Energ.*, **42**, 173-179. doi:10.1016/j.renene.2011.07.048.

Guo, Q., Zhou, L. and Wang, Z. (2015), "Comparison of BEM-CFD and full rotor geometry simulations for the performance and flow field of a marine current turbine", *Renew. Energ.*, **75**, 640-648. doi:10.1016/j.renene.2014.10.047.

Hansen, M.O. (2015), "Aerodynamics of wind turbines", *Routledge Taylor Fr. Gr.*, 1-189. doi:10.1002/0470846127.

Huang, B. and Kanemoto, T. (2015), "Multi-objective numerical optimization of the front blade pitch angle distribution in a counter-rotating type horizontal-axis tidal turbine", *Renew. Energ.*, **81**, 837-844. doi:10.1016/j.renene.2015.04.008.

Karthikeyan, T., Avital, E.J., Venkatesan, N. and Samad, A. (2017), "Design and analysis of a marine current turbine", *Proceedings of the ASME 2017 Gas Turbine India Conference, GTINDIA 2017* doi:10.1115/GTINDIA2017-4912.

Kinnas, S.A., Xu, W., Yu, Y.H. and He, L. (2012), "Computational methods for the design and prediction of performance of tidal turbines", *J. Offshore Mech. Arct. Eng.*, **134**, 011101. doi:10.1115/1.4003390.

Kolekar, N. and Banerjee, A. (2013), "A coupled hydro-structural design optimization for hydrokinetic turbines", *J. Renew. Sust. Energ.*, **5**. doi:10.1063/1.4826882.

Koo, G.W., Lee, S.M. and Kim, K.Y. (2014), "Shape optimization of inlet part of a printed circuit heat exchanger using surrogate modeling", *Appl. Therm. Eng.*, **72**, 90-96. doi:10.1016/j.applthermaleng.2013.12.009.

Lee, H., Jo, Y., Lee, D.J. and Choi, S. (2016), "Surrogate model based design optimization of multiple wing sails considering flow interaction effect", *Ocean Eng.*, **121**, 422-436. doi:10.1016/j.oceaneng.2016.05.051.

Leroux, T., Osbourne, N. and Groulx, D. (2019), "Numerical study into horizontal tidal turbine wake velocity de fi cit : Quasi- steady state and transient approaches", *Ocean Eng.*, **181**, 240-251. doi:10.1016/j.oceaneng.2019.04.019.

Liu, J., Lin, H., Purimitla, S.R. and Das E.T, M. (2017), "The effects of blade twist and nacelle shape on the performance of horizontal axis tidal current turbines", *Appl. Ocean Res.*, **64**, 58-69. doi:10.1016/j.apor.2017.02.003.

Menter, F.R. (1994), "Two-equation eddy-viscosity turbulence models for engineering applications", *AIAA J.*, **32**, 1598-1605. doi:10.2514/3.12149.

Moriarty, P.J. and Hansen, A.C. (2005), "AeroDyn theory manual", *Renew. Energ.*, **15**, 500-36313. doi:10.1146/annurev.fl.15.010183.001255.

Morris, C.E., O'Doherty, D.M., Mason-Jones, A. and O'Doherty, T. (2016), "Evaluation of the swirl characteristics of a tidal stream turbine wake", *Int. J. Mar. Energy*, **14**, 198-214. doi:10.1016/j.ijome.2015.08.001.

Myers, L. and Bahaj, A.S. (2007), "Wake studies of a 1/30th scale horizontal axis marine current turbine", *Ocean Eng.*, **34**, 758-762. doi:10.1016/j.oceaneng.2006.04.013.

Nishino, T. and Willden, R.H.J. (2012), "Effects of 3-D channel blockage and turbulent wake mixing on the limit of power extraction by tidal turbines", *Int. J. Heat Fluid Fl.*, **37**, 123-135. doi:10.1016/j.ijheatfluidflow.2012.05.002.

Priegue, L. and Stoesser, T. (2016), "The influence of blade roughness on the performance of a vertical axis tidal turbine", *Submitted to Int. J. Mar. Energy*, **17**, 136-146. doi:10.1016/j.ijome.2017.01.009.

Rahimian, M., Walker, J. and Penesis, I. (2018), "Performance of a horizontal axis marine current turbine– A comprehensive evaluation using experimental, numerical, and theoretical approaches", *Energy*, **148**, 965-976. doi:10.1016/j.energy.2018.02.007.

Ren, Y., Liu, B., Zhang, T. and Fang, Q. (2017), "Design and hydrodynamic analysis of horizontal axis tidal stream turbines with winglets", *Ocean Eng.*, **144**, 374-383. doi:10.1016/j.oceaneng.2017.09.038.

Rosli, R., Norman, R. and Atlar, M. (2016), "Experimental investigations of the Hydro-Spinna turbine performance", *Renew. Energy*, **99**, 1227–1234. doi:10.1016/j.renene.2016.08.034.

Samad, A., Kim, K.Y., Goel, T., Haftka, R.T. and Shyy, W. (2008), "Multiple surrogate modeling for axial compressor blade shape optimization", *J. Propuls. Power*, **24**, 301-310. doi:10.2514/1.28999.

Schleicher, W.C., Riglin, J.D. and Oztekin, A. (2015), "Numerical characterization of a preliminary portable micro-hydrokinetic turbine rotor design", *Renew. Energy*, **76**, 234-241. doi:10.1016/j.renene.2014.11.032.

Schluntz, J. and Willden, R.H.J. (2015), "The effect of blockage on tidal turbine rotor design and performance", *Renew. Energ.*, **81**, 432-441. doi:10.1016/j.renene.2015.02.050.

Subhra Mukherji, S., Kolekar, N., Banerjee, A. and Mishra, R. (2011), "Numerical investigation and evaluation of optimum hydrodynamic performance of a horizontal axis hydrokinetic turbine", *Renew. Sust. Energ.*, **3**. doi:10.1063/1.3662100.

Tahani, M., Babayan, N., Astaraei, F.R. and Moghadam, A. (2015), "Multi objective optimization of horizontal axis tidal current turbines, using Meta heuristics algorithms", *Energy Convers. Manage*, **103**, 487-498. doi:10.1016/j.enconman.2015.06.086.

Tian, W., Song, B., VanZwieten, J.H., Pyakurel, P. and Li, Y. (2016a), "Numerical simulations of a horizontal axis water turbine designed for underwater mooring platforms", *Int. J. Nav. Archit. Ocean Eng.*, **8**, 73-82. doi:10.1016/j.ijnaoe.2015.10.003.

Tian, W., VanZwieten, J.H., Pyakurel, P. and Li, Y. (2016b), "Influences of yaw angle and turbulence intensity on the performance of a 20 kW in-stream hydrokinetic turbine", *Energy*, **111**, 104-116. doi:10.1016/j.energy.2016.05.012.

Turnock, S.R., Phillips, A.B., Banks, J. and Nicholls-Lee, R. (2011), "Modelling tidal current turbine wakes using a coupled RANS-BEMT approach as a tool for analysing power capture of arrays of turbines", *Ocean Eng.*, **38**, 1300-1307. doi:10.1016/j.oceaneng.2011.05.018.

Vennell, R. (2013), "Exceeding the Betz limit with tidal turbines", *Renew. Energ.*, **55**, 277-285. doi:10.1016/j.renene.2012.12.016.

Wei, X., Huang, B., Liu, P., Kanemoto, T. and Wang, L. (2015), "Experimental investigation into the effects of blade pitch angle and axial distance on the performance of a counter-rotating tidal turbine", *Ocean Eng.*, **110**, 78-88. doi:10.1016/j.oceaneng.2015.10.010.

Zhu, B., Sun, X., Wang, Y. and Huang, D. (2017), "Performance characteristics of a horizontal axis turbine with fusion winglet", *Energy*, **120**, 431-440. doi:10.1016/j.energy.2016.11.094.

Zhu, G.J., Guo, P.C., Luo, X.Q. and Feng, J.J. (2012), "The multi-objective optimization of the horizontal-axis marine current turbine based on NSGA-II algorithm", *Proceedings of the IOP Conf. Ser. Earth Environ. Sci.*, **15**, 42039. doi:10.1088/1755-1315/15/4/042039.

QM

Nomenclature

Abbreviations

BEM	Blade element momentum
CAD	Computer-aided design
CFD	Computational fluid dynamics
KRG	Kriging
GA	Genetic algorithm
LE	Leading edge
MCT	Marine current turbine
NSGA II	Non dominated sorting genetic algorithm
PRESS	Predicted error sum of squares
PS	Pressure side
RANS	Reynolds-averaged Navier-Stokes
RBF	Radial basis function
RSA	Response surface approximation
SBO	Surrogate-based optimization
SS	Suction side
SST	Shear stress transport
TE	Trailing edge
TOPT	Optimized turbine
TREF	Reference turbine
TSR	Tip speed ratio

Symbols

a	Axial induction factor
a'	Tangential induction factor
C_D	Drag coefficient
C_L	Lift coefficient
C_P	Power coefficient
$C_{P(Peak)}$	Peak power coefficient
C_{PR}	Pressure coefficient
$C_{PR(\max)}$	Maximum pressure coefficient
c	Chord (m)
F	Objective function
k	Turbulent kinetic energy
NR	Number of rotor blades
P_{out}	Power output (W)
Q	Torque (N-m)
R	Rotor radius (m)
r	Local radius (m)
t	Thickness (m)
U_T	Free stream velocity (m/s)

w_0	Weight coefficient
w_i	Bias term
α	Angle of attack (^{o})
ß	Twist angle (^{o})
ρ	Density (kg/m^3)
σ^*	Cavitation ratio
Ω	Angular velocity of rotor (rad/s)
θ	Blade-pitch angle (^{o})
ω	Specific rate of dissipation
ε	Turbulent dissipation

Subscripts

ERR	Error
SUR	Surrogate